Flow Characteristics of Slat Cove Fillers

Hasan Kamliya Jawahar[a,*], Raf Theunissen[a,**], Mahdi Azarpeyvand[a], Carlos R. Ilário da Silva[b]

[a] *University of Bristol, Bristol, United Kingdom, BS8 1TR*
[b] *Embraer, Sáo José dos Campos, SP 12227-901, Brazil*

Abstract

Experimental measurements using Particle Image Velocimetry were carried out to understand the flow characteristics of a 30P30N high-lift airfoil with and without slat cove fillers. The tests were carried out for the 30P30N airfoil with a retracted chord of $c = 0.35$, at angles of attack of $\alpha = 6^\circ$ and 12°, and for a chord-based Reynolds number of $Re_c = 7.0 \times 10^5$. The wall pressure fluctuation results show that the use of slat cove fillers eliminates the slat tonal noise component. The results of the mean flow fields such as the normalized mean velocity, Reynolds stress components, and turbulent kinetic energy are presented for the baseline, half-slat cove filler, and slat cove filler configurations. The velocity contour results with streamlines showed a recirculation region within the slat cavity. The use of the half-slat cove filler reduced the size of the recirculation region and the use of the slat cove filler eliminated the recirculation region. The mean velocity and turbulent kinetic energy profiles at the slat wake showed no difference between the three tested configurations. The Particle Image Velocimetry results were further analyzed using Proper Orthogonal Decomposition. The results showed that the first two eigenmodes of the vorticity with the highest energy were contained within the slat shear layer and vortex shedding emanating from the slat cusp for the baseline case. The energy levels were distributed over the slat shear layer for the half-slat cove filler and slat cove filler configurations as the vortex shedding is suppressed by the use of the slat cove fillers.

Keywords: 30P30N, Experiment, Flow Structure, High-lift, Slat cove filler.

*Research Associate, Department of Aerospace Engineering
**Senior Lecturer, Department of Aerospace Engineering
Corresponding Author, Professor in Aeroacoustics, Department of Mechanical Engineering
Technology Development Engineer, Embraer
Email addresses: hasan.kj@bristol.ac.uk (Hasan Kamliya Jawahar), r.theunissen@bristol.ac.uk (Raf Theunissen), m.azarpeyvand@bristol.ac.uk (Mahdi Azarpeyvand), carlos.ilario@embraer.com.br (Carlos R. Ilário da Silva)

1. Introduction

Aircraft noise has remained an environmental issue since the entry of turbofan and turbojet engines into civil aviation. Even though the introduction of high bypass ratio turbofan engines has cut down the engine noise substantially, high levels of airframe noise still remains a problem, especially during the landing phase. High-lift device noise, especially slat noise is one of the dominant sources of airframe noises. Several passive and active flow control methods have been investigated in the past to attenuate airframe noise, the methods include morphing structures [1–4, 28–31], porous materials [5–7], surface treatments [8] and serrations [9].

Aeroacoustic studies on conventional slat and wing configurations have shown that it comprises of both the broadband and tonal noise components. Several studies on slat noise have shown several discrete tones at mid-frequency range [10–22]. However, their aeroacoustic mechanism is yet to be fully understood. These tonal peaks decrease with the angle of attack but their amplitude decreases with increasing slat gap and overlap [16]. Several experimental and computational studies [23–27] were carried out over the past decade to reduce the broadband noise arising from the slat cove region by filling the recirculation area within the slat cove gap. The approach of filling the slat cove gap to reduce the noise is based on eliminating the strong shear layer created after the cusp and avoiding the development of complicated flow structure within the slat cove region by using a smoothly contoured profile. Horne *et al.* [23] showed slat noise reductions of up to $4-5$ dB can be achieved by eliminating the unsteady recirculation within the slat cove region with the use of slat cove filler (SCF). Streett *et al.* [24] further investigated the aerodynamic and aeroacoustic characteristics of the SCF and showed noise reduction to be sensitive to the angle of attack and as well as the SCF profile. The SCF showed a noise reduction of up to 3-5 dB over a wide spectrum relative to the baseline. The results also showed improved aerodynamic performance for the SCF at angles of attack lower than 20°, however, the stall occurred 2 degrees earlier for the SCF compared to baseline.

Imamura *et al.* [25] and Ura *et al.* [26] showed that the use of a SCF can affect the lift characteristics of the high-lift airfoil in spite of achieving noise reduction up to 5 dB. They showed that the shape of the SCF profile plays an important role in the aerodynamic characteristics of the high-lift airfoil with cases with larger SCF stalling prematurely. Tao and Sun [27] performed an optimization study using computational methods with 44 SCF profile designs aimed to produce maximum lift coefficient for a fixed design point with the angle of attack of 22° and $Re_c = 9 \times 10^6$. The results showed smaller SCF profile can achieve high levels of noise reductions while maintaining the aerodynamic performance of the high-lift device.

More recently, the authors [28–31] have performed detailed aerodynamic and aeroacoustic study for 30P30N airfoil fitter with Half-slat cove fillers (H-SCF) and SCF. The study showed that the H-SCF and SCF configurations can maintain the same aerodynamic behavior as that of the baseline while portraying substantial levels of noise reduction of up to 5 dB. The acoustic results showed that the H-SCF and SCF configurations can eliminate the characteristic tonal peaks of the slat along with a reduction in broadband noise levels.

The noise reduction capabilities of the slat cove filler along with basic aerodynamic and noise measurements were considered in some recent studies. However, a detailed experimental study of the flow characteristics of such configuration and the interaction of the slat wake over the main-element of the high-lift airfoil with the slat cove fillers have not yet been reported. As part of the current study, wall pressure fluctuations, Particle Image Velocimetry measurements and analysis using Proper Orthogonal Decomposition method for a high-lift airfoil with and without slat cove filler will be investigated in detail. This can help better understand the mechanism leading to the suppression of the aerodynamic noise from the slat region while maintaining the aerodynamic performance of the high-lift device.

2. Experimental Setup

2.1. Airfoil and Wind-tunnel Setup

The aerodynamic measurements of the 30P30N three-element high-lift airfoil were carried out in the low-turbulence wind-tunnel facility at the University of Bristol. The tests were performed for three configurations, namely Baseline, Half-slat cove filler (H-SCF) and slat cove filler (SCF), as shown in Table **??**. The 30P30N three-element high-lift airfoil has a retracted chord of $c = 0.35$ m, slat chord $c_s = 0.15c$ and a span of $l = 0.53$ m. The other geometrical properties are the generic parameters used for a 30P30N high-lift airfoil [28–31]. The cartesian coordinate system (x, y, z) starts from the leading edge point of the retracted 30P30N airfoil as shown in Table **??**. In order to maintain two-dimensionality within the slat cove region, no brackets were used in the spanwise direction. The airfoil was made from aluminum and all the three-elements were held together by steel clamps on the sides of the airfoil. For high-lift airfoils, the installation effect and the flow three-dimensionalities affect both the aerodynamic and aeroacoustic measurements considerably. Studies have shown that the use of wind-tunnel boundary layer control to provide the average flow more two-dimensional on the airfoil, thus reducing uncertainties on the wing effective angle of attack [32]. However, no such treatments were used in the present study, so the results are presented for the tested geometric angle of attack in the low-turbulence wind-tunnel facility at the University of Bristol. The low-turbulence wind-tunnel facility has an octagonal working section of 0.8 m $\times$ 0.6 m $\times$ 1 m and has a contraction ratio of 12:1. The wind-tunnel is capable of a maximum velocity of up to 100 m/s with turbulence levels as low as 0.05% [33]. The working section is constructed with interchangeable transparent glass windows facilitating optical access for laser-based measurements, such as Particle Image Velocimetry (PIV). The flow at the mid-span of the high-lift airfoil in the measurement region was found to be two-dimensional with the aid of spanwise distributed surface mounted FG-3329-P07 microphones.

2.2. Slat Cove Filler Design

Slat cove fillers (SCF) are used to reduce slat noise while maintaining the aerodynamic behavior. The SCF was designed using a similar strategy introduced by Imamura *et al.* [25, 26] for experimentation purposes. Initially, RANS steady-state simulations for the Baseline case were performed at the angle of attack 8° and

the profile with high turbulent kinetic energy (TKE) indicating the slat shear layer trajectory within the slat cove region was extracted and used to define the SCF profile (see Table **??**). Another configuration with a Half SCF (H-SCF) was also considered, which exhibits good aerodynamic and noise reduction properties as shown computationally by Tao [27]. Both the slat cove-fillers were manufactured using 3D printing technology in four different sections that could be slid along the span of the slat cove region.

2.3. Wall Pressure Measurement Setup

The unsteady surface pressure measurements were performed using remote sensing microphone probes made from Panasonic WM-61A microphones fitted using a custom made holder to a 1.6 mm diameter brass tube with 0.4 mm pinholes at streamwise location M1 ($x \times y \times z$ =15.126 mm×-5.839 mm×265 mm) shown in Table. **??**). The remote sensors are connected to the pressure tap brass tube using a plastic tubing with an inner and outer diameter of 0.8 mm and 4 mm [34]. The power spectrum of the wall pressure measurements was obtained using the power spectral density (PSD) of the pressure signals with the Hanning window. The acquired data were averaged for 200 times to yield a frequency resolution of Δf = 6.25 Hz. The sound pressure level (SPL) spectrum was calculated from $SPL = 20 \cdot log10(p_{rms}/p_{ref})$, where p_{rms} is the root-mean-square of the acoustic pressure and p_{ref} = 20 μPa is the reference pressure. The overall sound pressure level was resolved for a frequency range from f = 100 Hz to 32 kHz. The data were acquired for 120 seconds and sampled at 2^{15} Hz.

2.4. Particle Image Velocimetry Setup

The flow structure within and around the slat cove region of the three-element airfoil was studied using two-dimensional two-component PIV. A Dantec DualPower 200 mJ Nd:YAG laser with a wavelength of 532 nm was used to produce 1 mm thick laser sheet with a time interval between each snapshot of 9 μs and a repetition rate of 10 Hz. A mixture of Polyethylene glycol 80 with a mean diameter of 1 μm was used to seed the air inside the low turbulence wind tunnel. A total of 2400 images for each measurement were captured using a FlowSense 4 MP CCD camera with a resolution of 2078 × 2078 pixels and 14 bit. The corresponding field view around the slat region was 6.3 cm × 6.3 cm. Two such windows within the slat cove and at the slat trailing edge were used to capture the flow field. The images were analyzed using the DynamicStudio software from Dantec. The iterative process yielded a grid correlation window of 16 × 16 pixels with an overlap of 50%, resulting in a final vector spacing of 0.23 mm.

2.5. Proper Orthogonal Decomposition Setup

In the present study, the *snapshot POD* method [35] is used on the dense vector fields acquired from the PIV measurements. This method is adopted as it uses the PIV snapshots for calculation making it computationally inexpensive. The instantaneous flow filed from the PIV measurement is considered as the PIV snapshot. The POD is calculated for 2400 PIV snapshots for each of the presented cases. The vectors in the PIV shadow region were masked to eliminate any discrepancies caused by inaccurate vector fields in the

A schematic of the 30P30N Baseline airfoil fitted with half-slat cove filler (H-SCF) and slat cove filler (SCF) listed with the slat trailing-edge wake measurement locations.

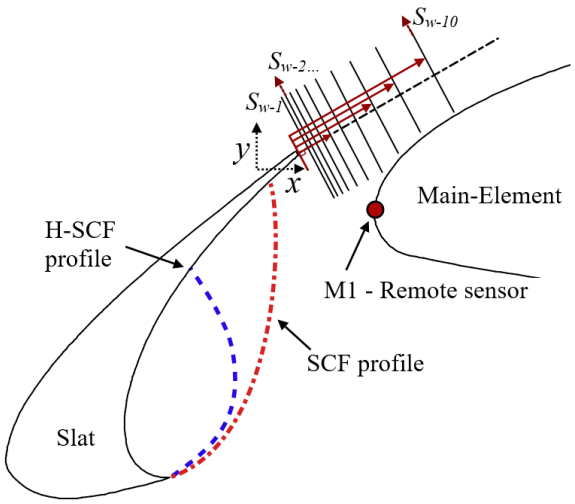

Designation	x (mm)
S_{w-1}	15.0
S_{w-2}	19.9
S_{w-3}	26.5
S_{w-4}	35.3
S_{w-5}	46.9
S_{w-6}	62.4
S_{w-7}	82.9
S_{w-8}	110.3
S_{w-9}	147.0
S_{w-10}	195 .0

shadow region. In the current study, the POD modes are calculated, not only based on the velocity data, but also for the vorticity of the flow field for both the tested configurations for the angles of attack $\alpha = 6°$ and $12°$ at a chord-based Reynolds number of $Re_c = 7.5 \times 10^5$. In the current work, the vorticity was calculated based on a second-order least-squares fit of the form $ax^2 + by^2 + cxy + dx + ey + f$ to the data pertaining to each of the velocity components. The latter subsequently allowed a straightforward evaluation of the spatial gradients and hence, vorticity.

At first, the calculated mean velocity and vorticity fields are considered as the zeroth mode of the POD. All the fluctuating flow field components are used for the rest of the analysis are arranged in a matrix $\mathbf{U}$ as [36, 37],

$$\mathbf{U} = [\mathbf{u}^1\mathbf{u}^2...\mathbf{u}^N] = \begin{bmatrix} u_1^1 & u_1^2 & ... & u_1^N \\ \vdots & \vdots & \vdots & \\ u_M^1 & u_M^2 & ... & u_M^N \\ v_1^1 & v_1^2 & ... & v_1^N \\ \vdots & \vdots & \vdots & \\ v_M^1 & v_M^2 & ... & v_M^N \\ w_1^1 & w_1^2 & ... & w_1^N \\ \vdots & \vdots & \vdots & \\ w_M^1 & w_M^2 & ... & w_M^N \end{bmatrix}, \tag{1}$$

where u, v and w are the three fluctuating velocity components, N is the number of snapshots and M is the

positions of the velocity vectors in a given snapshot. The autocovariance matrix is created as

$$\tilde{\mathbf{C}} = \mathbf{U}^T\mathbf{U}, \tag{2}$$

and the corresponding eigenvalue problem can be solved by,

$$\tilde{\mathbf{C}}\mathbf{A}^i = \lambda^i\mathbf{A}^i. \tag{3}$$

The solutions of which are arranged by the size of the eigenvalues,

$$\lambda^1 > \lambda^2 > \lambda^3 > ... > \lambda^N = 0. \tag{4}$$

The resultant eigenvectors from Eq. 3 are used to construct the POD modes Φ^i,

$$\Phi^i = \frac{\sum_{n=1}^{N} A_n^i \mathbf{u}^n}{\left\| \sum_{n=1}^{N} A_n^i \mathbf{u}^n \right\|}, \qquad i = 1, 2..., N, \tag{5}$$

where A_n^i is the n^{th} component of the non-dimensional eigenvector corresponding to λ^i eigenvalue from Eq. 3.

The original snapshots of the flow field are expanded in a series of POD modes with expansion coefficients a^i for each POD mode i. The expansion of the fluctuating part of a snapshot n is as follows,

$$\mathbf{u}^n = \sum_{i=1}^{N} a_i^n \Phi^i = \mathbf{\Psi}\mathbf{a}^n, \tag{6}$$

where $\mathbf{\Psi} = [\Phi^1\Phi^2\Phi^3...\Phi^N]$. The POD coefficients can be determined by projecting the fluctuating flow fields onto the POD modes,

$$\mathbf{a}^n = \mathbf{\Psi}^T\mathbf{u}^n. \tag{7}$$

The energy of a fluctuating flow field in a snapshot for a given POD-mode is proportional to the corresponding eigenvalue. The first mode represents the most energetic structure of the flow and it is usually associated with the large scale flow structures. The first POD mode is the most important in terms of energy as ensured by the arrangement of the eigenvalues and eigenvectors in Eq. 4. Therefore, the first few modes are sufficient to investigate the dominant flow features [36, 37].

3. Results and Discussion

The noise generated by high-lift devices are one of the dominant components of the airframe noise. The complex tonal and broadband noise generation mechanisms of slats [14–22] largely dependant on the geometry and configuration. Studies [18, 38] have shown similarities in the tonal noise seen in rectangular cavities to slat with the feedback mechanism between the unsteady vortices emanating from the slat cusp and the trailing edge acting as a resonator leading to the flow induced cavity oscillations with the vortical disturbances driving the oscillations.

3.1. Wall Pressure Measurement Analysis

Near-field wall pressure fluctuation results are presented to gain an insight into the noise suppression mechanism of the slat cove fillers. The unsteady surface pressure measurements were acquired at various spanwise locations on the surface of the main-element of the high-lift airfoil. The measurements are presented for location M1 detailed in Table. **??**. The results are presented for angles of attack of $\alpha = 6°$ and $12°$ corresponding to the PIV measurements presented in the following section. The sound pressure levels are presented in terms of the slat based Strauhal number ($St_s = f \times c_s/U_\infty$). Previous studies [39] have shown that the wall pressure fluctuation on the main-element is sufficient to accurately predict the slat tones and provide some useful information about the broadband energy content of the flow structures within the slat cove. The results from the unsteady wall pressure measurements from the remote sensor M1 at the leading edge of the main-element are shown in Fig. 1. The dominant tonal characteristics of the wall pressure spectra evidently seen at both the presented angles of the attack indicate the presence of cavity oscillations. The wall pressure fluctuation spectra result for the Baseline case in Fig. 1 show multiple distinct narrowband peaks with $St_s = 1.45$ at the angle of attack $\alpha = 6°$ and $St_s = 1.6\&3.2$ at the angle of attack $\alpha = 12°$, characterizing cavity oscillations.

The results of the H-SCF and SCF configurations clearly show that it is of broadband in nature with the tonal component eliminated. The wall pressure spectra at the angle of attack $\alpha = 6°$, for the H-SCF, show an increase of about 3.5 dB at low-frequency range $St_s < 1$ compared to the Baseline and the SCF configuration. The results for the SCF configuration show a reduction of up to 5 dB for $2 < St_s > 6$ compared to the Baseline and H-SCF. At the angle of attack $\alpha = 12°$, the results show an increase of up to 5 dB at about $St_s < 0.6$ for the SCF configuration compared to the Baseline and H-SCF configuration. However, at $St_s > 0.6$ reductions of up to 7 dB can be observed for the SCF configuration compared to the Baseline and H-SCF. Overall the results show that the configurations with slat cove fillers not only eliminates the tonal noise component but also reduces the broadband noise component.

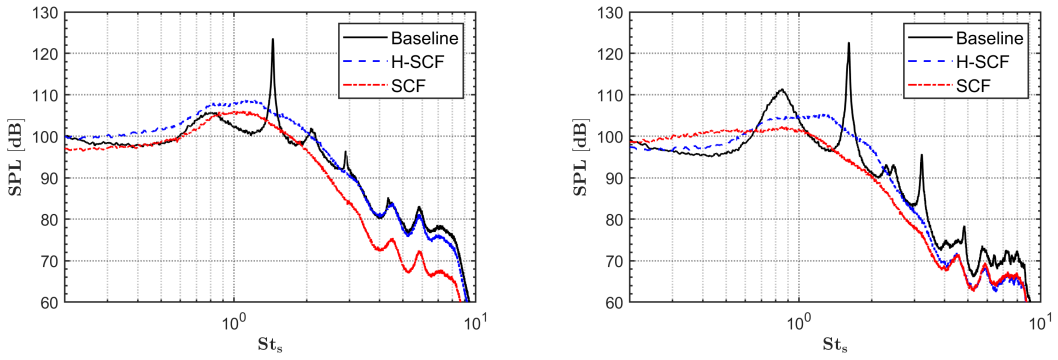

(a) $\alpha = 6°$ (b) $\alpha = 12°$

Figure 1: Near field wall pressure fluctuation for the remote surface pressure transducers M1 at the freestream velocity $U_\infty = 30$ m/s ($Re_c = 7.0 \times 10^5$).

3.2. Particle Image Velocimetry Analysis

Detailed Particle Image Velocimetry (PIV) studies were performed in and around the slat region for the Baseline, H-SCF, and SCF configurations at the geometric angles of attack $\alpha = 6°$, $8°$, $10°$ and $12°$ with a free-stream velocity of $U_\infty = 30$ m/s ($Re_c = 7.0 \times 10^5$). For the purpose of brevity, the results are presented only for $\alpha = 6°$ and $12°$ in Figs. 2 and 3, respectively. The figures are presented in a table format with the columns showing the different slat configurations and the rows showing different flow field components. The contours of the non-dimensional mean streamwise (U/U_∞) and crosswise (V/V_∞) velocity distribution around the slat region, with overlaid streamlines, are shown in the first and second row respectively, in Figs. 2 and 3. For the Baseline airfoil, the streamlines show that the shape and structure of the recirculation region present within the slat cove region is largely influenced by the angle of attack. The magnitude of the negative streamwise velocity that arises right after the flow impingement ($x/c \approx 0.05$) on the main-element appears to be influencing the trajectory of the slat shear layer leaving the slap cusp. The trajectory of the slat shear layer is also influenced by the angle of attack.

At $\alpha = 6°$, the recirculation region within the slat cavity appear to be the largest with the longest slat shear layer trajectory, which impinges much closer to the slat trailing-edge and most of the flow after the impingement moves toward the slat trailing-edge and mixes into the free-stream. The impingement point of the slat shear layer on the slat lower surface moves away from the slat trailing-edge toward the slat mid-chord location as the angle of attack is increased. This slat shear layer trajectory with a much shorter path before the impingement restricts the recirculation area at increased angles of attack. This decreases the recirculation area resulting in the higher vortex velocity and it also increases the crosswise velocity inside the slat cove region. The increased flow through the slat gap along with the higher negative streamwise velocity at the main-element impingement region appears to be the key factors influencing the movement of the slat shear layer trajectory with the changes in the angle of attack. The contours show negative velocity inside the slat cove region, which can be associated with the vortices. The highest negative streamwise velocity on the slat lower surface at $\alpha = 12°$ implies highest vortex velocity amongst the tested angles of attack. The highest streamwise velocity on the upper side can be seen for $\alpha = 12°$ over the main-element right after the slat gap, where the velocity reaches up to twice as much as that of the inlet velocity. The highest velocity on the lower side occurs near the slat cusp where the slat shear layer originates. For the Baseline case, the maximum value of the crosswise velocity occurs at the slat gap region with increased velocity seen at $\alpha = 12°$ compared to all the other angles of attack. The maximum crosswise velocity lies between the free slat shear layer and the main-element of the 30P30N airfoil for all the presented angles of attack.

The effects of the H-SCF and SCF on the mean flow structures and velocities within the slat cove region are minimal as the shape and trajectory of the slat shear layer follows the same trend as that of the Baseline for all the tested angles of attack. However, the size of the vortical structures inside the slat cove region is reduced noticeably. The use of the slat cove filler leads to the elimination of the large flow recirculation within the slat cove region as the available area for recirculation is occupied by the cove fillers. However,

closer to the slat trailing-edge, on the lower surface of the SCF, smaller recirculation region has emerged. Similar to the Baseline airfoil, the size and magnitude of these recirculation regions are clearly influenced by the angle of attack. The recirculation region also arises right after the impingement of the slat shear layer onto the slat lower surface, as previously seen in the case of the Baseline airfoil.

Olson *et al.* [38] showed that the favorable pressure gradient between the slat upper and lower surface at the slat cusp accelerates and energizes the flow, which also influences the strength and trajectory of the slat shear layer. The cove filler configurations have completely eliminated this favorable pressure gradient at the slat cusp, thus reducing the energy of the existing limited shear layer. The existing smaller recirculation region can be completely eliminated by having an SCF profile that follows the same profile as that of the slat shear layer trajectory. However, this could prove difficult for practical operation as this slat shear layer trajectory is not only dependant on the angle of attack but also on the operating Reynolds and Mach numbers. If the SCF profile is larger than the slat shear layer profile then the flow at the slat gap gets restricted, which consequently affects the suction peak and aerodynamic performance of the main-element. Nevertheless, an SCF profile that eliminates the large recirculation region within the slat cove, while maintaining the aerodynamic performance at the same time is highly favorable as they are viable sources of noise reduction, as shown by Imamura *et al.* [25, 26], Tao [27] and also by the authors in [28–31].

The non-dimensional streamwise ($\overline{u'u'}/U_\infty^2$) and crosswise ($\overline{v'v'}/U_\infty^2$) Reynolds normal stress tensors around the slat region for the Baseline, H-SCF and SCF configurations for all the tested angles of attack are presented in the third and fourth row respectively, in Figs. 2 and 3. The presented results of the normal Reynolds stress components ($\overline{u'u'}$ and $\overline{v'v'}$) show that the crosswise Reynolds normal stress components ($\overline{v'v'}$) are higher than that of the streamwise Reynolds normal stress components ($\overline{u'u'}$) for all the presented configurations and angles of attack. The maximum value of the $\overline{u'u'}$ components for all the configurations can be found at the originating location of the slat shear layer adjacent to the slat cusp and also at the vicinity of the slat trailing edge. The maximum value of the $\overline{v'v'}$ components can be observed at the slat gap region close to the suction side of the main-element for both the Baseline and the H-SCF configurations. However, the $\overline{v'v'}$ components for the SCF configuration is slightly reduced at the slat gap region but increased values of it can be observed on the lower surface of the SCF itself. Similar behavior can be observed for all the presented angles of attack. The results also show that the shear stress distribution for both the normal eddy stress components ($\overline{u'u'}$ and $\overline{v'v'}$) reduces as the angle of attack is increased for all the three configurations.

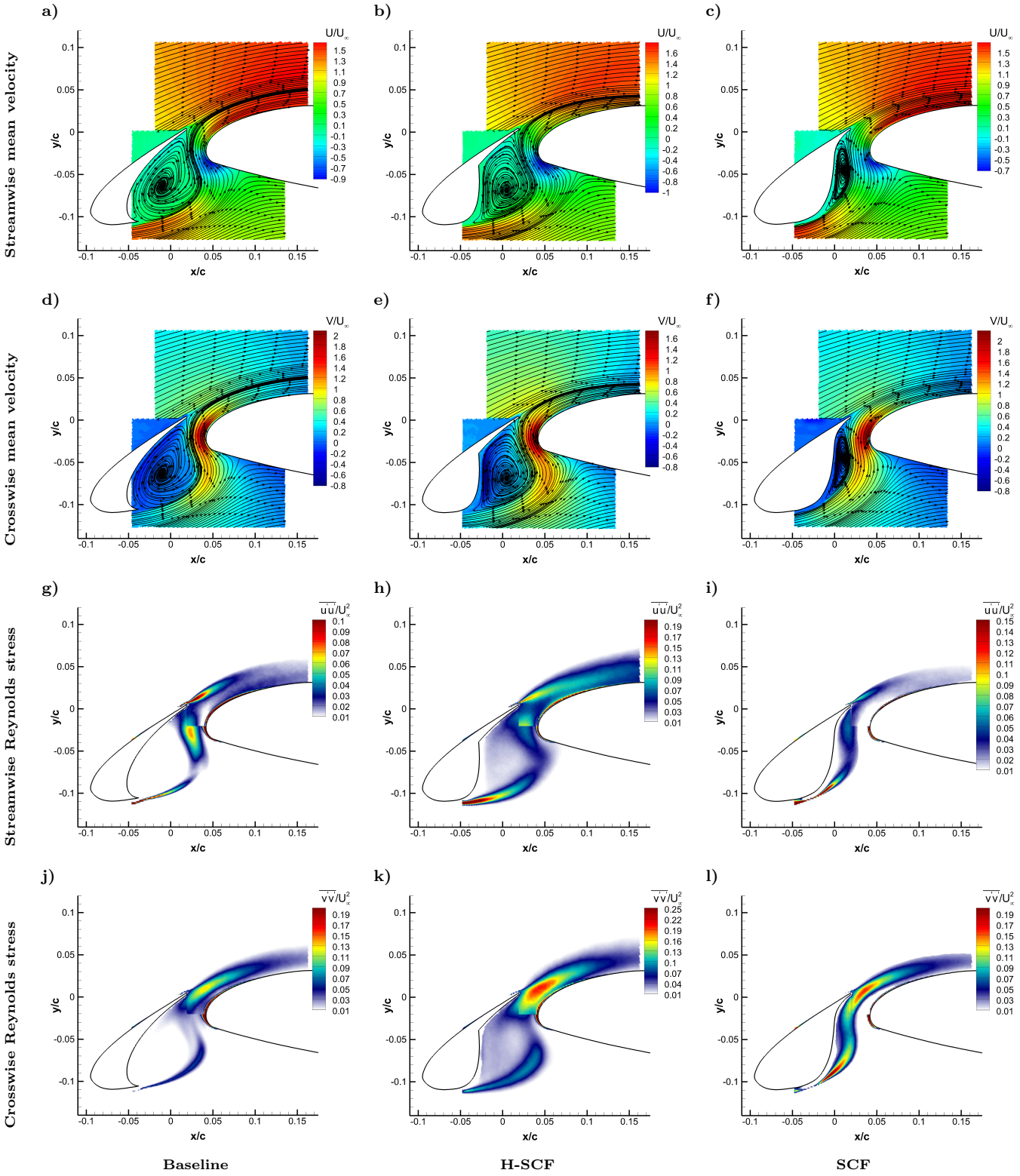

Figure 2: Contours of the mean velocity components along with Reynolds stress tensors around the slat region for $\alpha = 6^\circ$ with a freestream velocity of $U_\infty = 30$ m/s, $Re_c = 7.0 \times 10^5$.

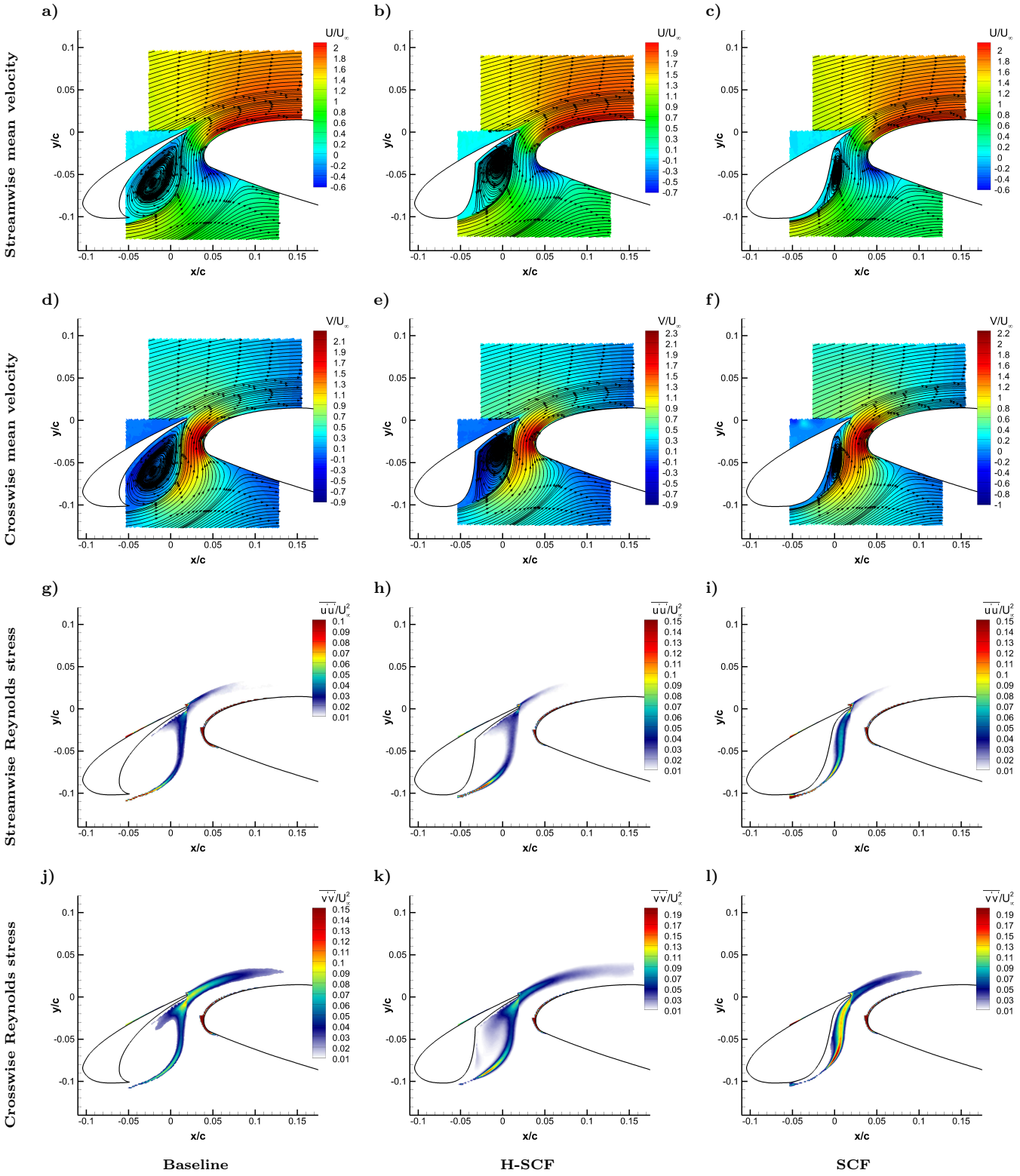

Figure 3: Contours of the mean velocity components along with Reynolds stress tensors around the slat region for $\alpha = 12^\circ$ with a freestream velocity of $U_\infty = 30$ m/s, $Re_c = 7.0 \times 10^5$.

The slat wake development at various near and far slat wake locations (see Table. **??**) for the Baseline, H-SCF, and SCF configurations are presented for the angles of attack $\alpha = 6^\circ$ and 12° in Figs. 4 and 5, respectively. The results of the mean velocity and TKE profiles are presented for eight streamwise locations at the near-wake location of the slat with the slat trailing-edge as the datum point in Figs. 4 and 5. The first six slat near-wake locations $x = 15.0$, 19.9, 26.5, 35.3, 46.9 and 62.4 mm ($S_{w-1,\ldots,6}$) are located between the slat trailing-edge and the main-element. The last four slat far-wake locations $x = 82.9$, 110.0, 147.0 and 195.0 mm ($S_{w-7,\ldots,10}$) are located within the slat wake just above the main-element. The results of the non-dimensional streamwise velocity (U/U_∞) at the angle of attack $\alpha = 6^\circ$ in Figs. 4a and 4b show a noticeable change for the slat wake profile of the H-SCF configuration toward the lower side of the slat-trailing edge with increased wake deficit compared to the Baseline and SCF configurations. This increased wake deficit on the lower side for the H-SCF also affects the velocity profile over the main-element as seen in Fig. 4b. The results for the SCF streamwise velocity profile follows a similar trend to that of the Baseline with negligible effects. The H-SCF slat wake also affects the flow above the main-element as seen at location $x = 82.9$ mm (S_{w-9}, see Fig. 4b). The strength of the slat wake above the main-element reduces at further downstream locations ($x > 147.0$ mm). The results of the TKE within slat wake in Figs. 4c and 4d clearly show increased TKE for the H-SCF compared to the Baseline and the SCF configurations at all the presented slat wake locations especially in the region below the slat trailing-edge and above the main-element, whereas, the results for the Baseline and the SCF case are very similar to each other. The use of H-SCF has evidently affected the shear layer and flow through the slat gap by reducing the flow velocity and increasing the TKE compared to the Baseline and SCF configurations at low angles of attack.

At the angle of attack $\alpha = 12^\circ$, the non-dimensional streamwise velocity results show insignificant differences between the three different configurations. The results show higher velocity at near wake locations (S_{w-1}, S_{w-2} and S_{w-3}) for $\alpha = 12^\circ$ relative to the $\alpha = 6^\circ$. The results of the non-dimensional streamwise velocity on the upper side of the slat wake reach up to $U/U_\infty = 1.3$ and on the lower side it reaches up to $U/U_\infty = 1$, whereas for $\alpha = 6^\circ$ non-dimensional streamwise velocity on the upper side of the slat wake reaches only up to $U/U_\infty = 1.2$. This shows that the flow has accelerated on the upper and lower side of the slat trailing-edge at $\alpha = 12^\circ$ relative to the $\alpha = 6^\circ$. At the increased angle of attack 12°, the results of the mean velocity field and the turbulent kinetic energy profiles show no change or insignificant change between the Baseline, H-SCF, and SCF configurations. The results here show that the use of H-SCF and SCF does not necessarily affect the flow at the slat wake and the boundary layer over the main-element. The slightly increased mean velocity components observed at the slat near-wake region for the H-SCF and SCF configurations also corresponds to the improved aerodynamic performance for the H-SCF and SCF configurations seen in the author's previous studies [28–31]. It is noteworthy that the H-SCF influence on the slat wake showed a tendency to increase as the angle of attack is decreased, whereas the H-SCF configuration showed a minor impact for the reported angles of attack.

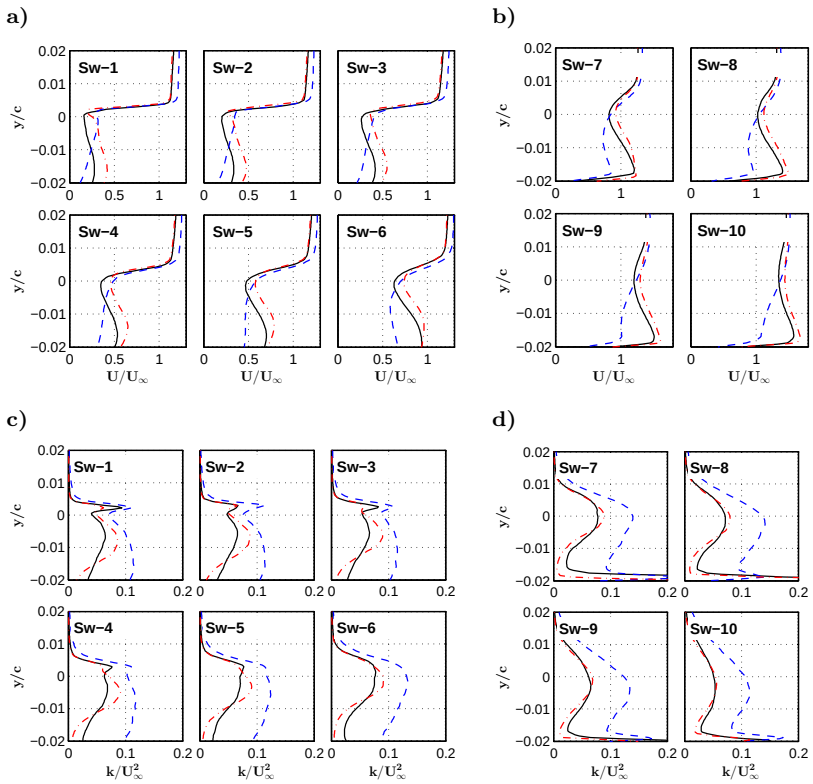

Figure 4: Mean velocity and turbulent kinetic energy profiles at the slat wake for $\alpha = 6°$ at the freestream velocity $U_\infty = 30$ m/s ($Re_c = 7.0 \times 10^5$), for Baseline ——, H-SCF – – and SCF –·–.

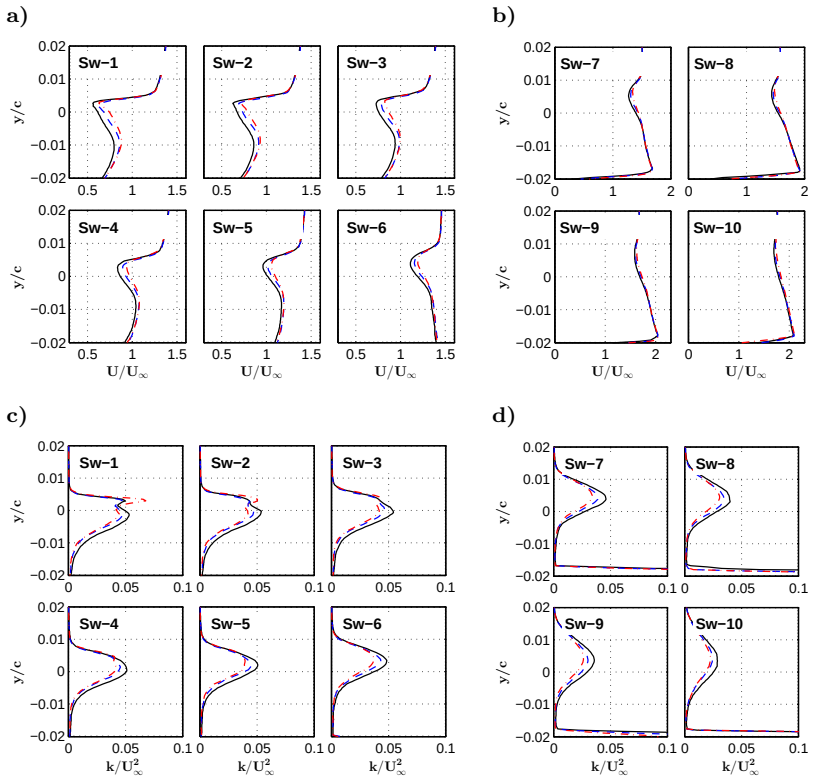

Figure 5: Mean velocity and turbulent kinetic energy at the slat wake for $\alpha = 12°$ at the freestream velocity $U_\infty = 30$ m/s ($Re_c = 7.0 \times 10^5$), for Baseline ——, H-SCF – – and SCF –·–.

3.3. Proper Orthogonal Decomposition Analysis

Proper Orthogonal Decomposition (POD) has shown to be an effective method for identifying dominant flow features, such as large coherent structures in a turbulent flow. The small turbulent flow motions often compile to make large-scale turbulent structures, which can be identified using the POD method. The POD analysis is best suited for problems that involve regular vortex shedding, such as the slat cove flow discussed in the present study. This method has been used by researchers for a variety of flow problems such as airfoils, cavities, bluff-bodies, and jets to isolate dominant periodic flow phenomena [40–44]. Previous studies [40–42] used POD to analyze the slat cove dynamics at several angles of attack at a chord-based Reynolds number of $Re_c = 6.5 \times 10^5 - 1.3 \times 10^6$, similar to that of the present study. The results showed the existence of small structures within the shear layer. It was also suggested that the presence of these smaller features within the shear layer itself and their movement past the slat and main-element would likely result in the generation of high-frequency noise levels.

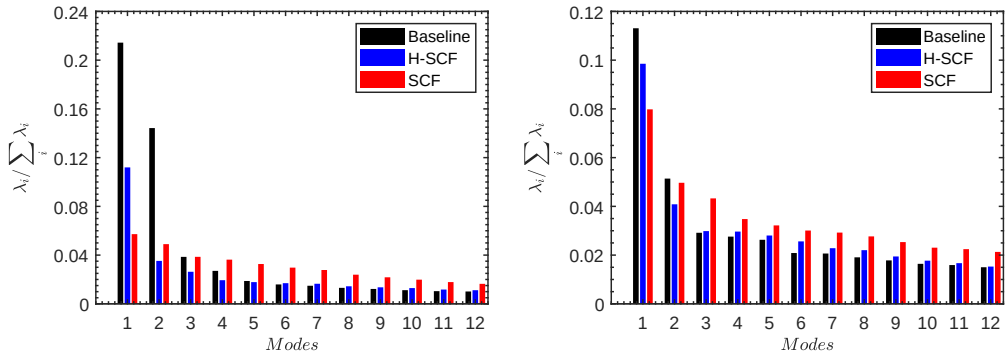

(a) $\alpha = 6°$ (b) $\alpha = 12°$

Figure 6: The eigenvalue distribution of the first 12 POD mode within the slat cove region and at the slat wake for angles of attack (a) $\alpha = 6°$ and (b) $\alpha = 12°$.

The number of resolved modes that contains 90% of the system's total energy for each of the configurations for the two angles of attack are presented in Table 1. The normalized eigenvalues for each of the first 12 POD modes within the slat cove region and at the slat wake for angles of attack $\alpha = 6°$ and $12°$ for all the tested configurations are presented in Fig. 6. The normalization was achieved by dividing each eigenvalue by the sum of all the eigenvalues. The eigenvalues provide an estimation of the coherent energy embedded within each of the vorticity POD modes [45]. For all the tested configurations the results show that a significant amount of energy is contained within the first two modes and the remaining energy is distributed over a wide range of modes portraying an exponential decay.

At the angle of attack $\alpha = 6°$, the first two modes are clearly dominant of the Baseline case in Fig. 6. The use of cove fillers substantially reduces the energy for the first two modes compared to the Baseline case, yet both the first two modes remain of equal importance for all the presented cases. For the first mode with the highest energy, the SCF has eigenvalues lower than that of H-SCF configuration but in the case of the second

Table 1: The number of resolved modes that contains 90% of the systems energy for each configuration.

α (deg.)	Baseline	H-SCF	SCF
6	593	759	751
12	737	759	598

mode, the H-SCF has lower eigenvalue than that of the SCF at $\alpha = 6°$ (Fig. 6a). The results also show that as the angle of attack is increased the flow becomes more turbulent and hence it requires more modes to be described accurately, which is reflected in the increased importance of the higher mode numbers (Fig. 6 and Table 1). This suggests the flow to become less temporally coherent and more turbulent requiring more modes to describe each individual flow field.

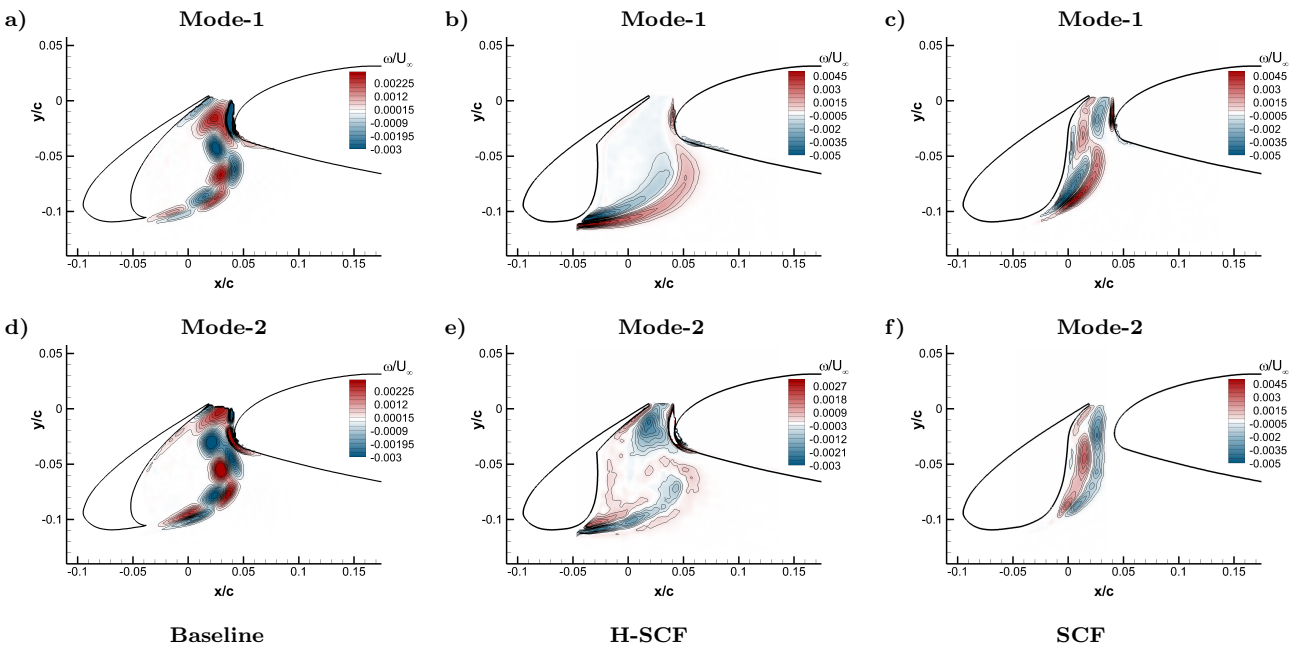

Figure 7: The non-demensionalized vorticity component of the first two POD modes within the slat cove region for $\alpha = 6°$ with a freestream velocity of $U_\infty = 30$ m/s, $Re_c = 7.0 \times 10^5$.

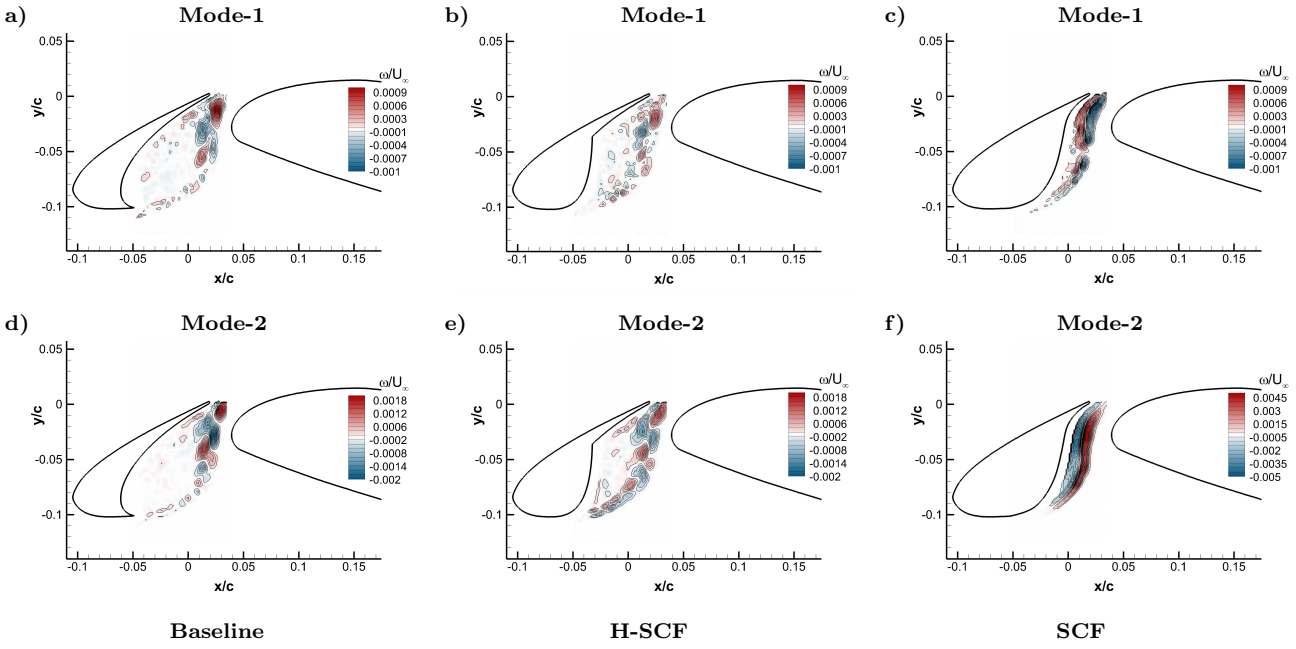

Figure 8: The non-demensionalized vorticity component of the first two POD modes within the slat cove region for $\alpha = 12°$ with a freestream velocity of $U_\infty = 30$ m/s, $Re_c = 7.0 \times 10^5$.

The results of the first two POD modes of the vorticity fields within the slat cove region are presented for the angles of attack $\alpha = 6°$ and 12° in Figs. 7 and 8, respectively. For mode-1 at $\alpha = 6°$, the alternating pattern of the large coherent structures for the Baseline indicates the presence of regular vortex shedding along the shear layer, which is absent at mode-1 for both the H-SCF and SCF configurations. This also corresponds to the tonal peak behavior observed for the Baseline case and the absence of the tones for the H-SCF and SCF in the wall pressure measurement results in Fig. 1. The vorticity contour results of the Baseline case clearly show that the first two modes with the higher energy contain the larger coherent structures from the vortex shedding. For H-SCF at $\alpha = 6°$, mode-1 clearly shows that the high energy shear layer does not move toward the slat trailing edge and into the slat gap unlike the Baseline and the SCF. The results for the first two POD modes for the H-SCF and SCF configurations at $\alpha = 6°$ show that the high energy is contained within the shear layer in the absence of the vortex shedding.

For the Baseline case at the angle of attack $\alpha = 12°$ at mode-1, the alternating pattern in the vorticity contours indicates the presence of a regular vortex shedding but with reduced energy compared to $\alpha = 6°$ (see Fig. 6). The structures of the mode distribution evidently show that the dominant flow feature is the slat cusp shear layer. The energy of the shear layer at mode-1 and 2 can be clearly seen to reduce for the H-SCF and SCF relative to the Baseline for all the presented angles of attack. The H-SCF case at angles of attack $\alpha = 12°$ show vortex shedding with smaller periodic structures with much-reduced energy compared to the Baseline case. The elimination of the sudden pressure difference at the slat cusp by the use of a small slat cove filler (H-SCF) evidently reduces the energy contained within the slat shear layer. For the SCF case, the energy and the periodicity in the vortex shedding process are clearly eliminated due to its interaction with the lower surface of the SCF. Overall, the results have shown that the use of slat cove fillers eliminates the vortex shedding and reduces the energy contained within the slat shear layer.

4. Conclusion

The flow structures within the slat cove for a 30P30N airfoil fitted with two different types of slat cove fillers are thoroughly investigated using near-field unsteady wall pressure measurements, Particle Image Velocimetry and analyzed using Proper Orthogonal Decomposition. The tests were conducted in the low turbulence wind tunnel at the University of Bristol for the 30P30N airfoil with a retracted chord of $c = 0.35$ at a chord-based Reynolds number of $Re_c = 7.0 \times 10^5$. The tests were carried out for angles of attack $\alpha = 6°$ and 12°. The near-field wall pressure fluctuations showed tonal behavior for the Baseline case, while the Half-Slat Cove Filler and the Slat Cove Filler configurations completely eliminated the tonal behavior with a notable reduction in the broadband noise signature. The contours of the normalized mean velocity fields showed that the shear layer path generated at the slat cusp for the Baseline case is highly influenced by the angle of attack. The use of the slat cove fillers is also observed to strongly influence the slat shear layer trajectory. A large recirculation region is observed within the slat cavity for the Baseline case. For the Half-Slat Cove Filler configuration, the size of the recirculation region is reduced by half. In the case of Slat Cove

Filler configuration, the recirculation region is almost completely eliminated for both the angles of attack. The use of slat cove fillers alters the shape and intensity of the recirculation region, which corresponds to the elimination of tonal behavior observed in the near-field wall pressure measurements. The slat wake flow field analysis has also shown that the use of slat cove fillers influences the slat wake behavior at low angles of attack of $\alpha = 6°$, with increased turbulent kinetic energy for Half-Slat Cove Filler configuration compared to the Baseline and Slat Cove Filler configuration. At the angle of attack $\alpha = 12°$, the results showed an insignificant difference in velocity and turbulent kinetic energy between the three configurations, which corresponds to the insignificant aerodynamic influence of the slat modifications. The Proper Orthogonal Decomposition results for all the presented cases show that the first two modes contained the highest energy compared to the other modes. The Baseline case possessed higher energy compared to the Half-Slat Cove Filler and Slat Cove Filler configuration for all the tested angles of attack. The contours of the vorticity eigenmodes showed higher energy within the slat shear layer emanating from the slat cusp and the presence of vortex shedding for the Baseline case at both the presented angles of attack. It was also observed that the use of the slat cove fillers eliminates the vortex shedding that in turn resulted in the energy levels distributed within the shear layer. The results in this study has shown that despite the significant flow modification and noise reduction achieved by the use of slat cove fillers, the flow remains unchanged downstream of the slat trailing edge keeping the confluent boundary layer over the high-lift airfoil intact.

References

[1] Kamliya Jawahar, H., Azarpeyvand, M., and Silva, C., "Aerodynamic and Aeroacoustic Performance of Airfoils Fitted with Morphing Trailing-edges", AIAA 2018-2815, 2018.

[2] Ai, Q., Kamliya Jawahar, H., and Azarpeyvand, M., "Experimental Investigation of Aerodynamic Performance of Airfoils Fitted with Morphing Trailing Edges", AIAA 2016-1563, 2016.

[3] Kamliya Jawahar, H., Ai, Q., and Azarpeyvand, M., "Experimental and Numerical Investigation of Aerodynamic Performance of Airfoils Fitted with Morphing Trailing Edges", AIAA 2017-3371, 2017.

[4] Kamliya Jawahar, H., Ai, Q., and Azarpeyvand, M., "Experimental and Numerical Investigation of Aerodynamic Performance of Airfoils with Morphed Trailing Edges", *Renewable Energy*, Vol. 127, 2018, pp: 355-367.

[5] Liu, H.R., Azarpeyvand, M., Wei, J.J., and Qu, Z.G., "Tandem Cylinder Aerodynamic Sound Control Using Porous Coating", *Journal of Sound and Vibration*, Vol. 334, 2015, pp: 190-201.

[6] Showkat Ali, S. A., Azarpeyvand, M., and Ilario, C., "Trailing Edge Flow and Noise Control using Porous Treatments", *Journal of Fluid Mechanics*, Vol. 850, 2018, pp: 83-119.

[7] Showkat Ali, S. A., Szoke, M., Azarpeyvand, M., and Ilario, C., "Turbulent Flow Interaction with Porous Surfaces", AIAA 2018-2801, 2018.

[8] Afshari, A., Azarpeyvand, M., Dehghan, A. A., and Szoke, M., "Trailing Edge Noise Reduction Using Novel Surface Treatments", AIAA 2016-2834, 2016.

[9] Liu, X., Kamliya Jawahar, H., Azarpeyvand, M., and Theunissen, R. "Aerodynamic Performance and Wake Development of Airfoils with Serrated Trailing Edges", *AIAA Journal*, Vol. 55, No. 11, 2017, pp: 3669-3680.

[10] Mendoza, J.M., Brooks, T.F., and Humphreys, W.M., "An Aeroacoustic Study of a Leading Edge Slat Configuration", *International Journal of Aeroacoustics*, Vol. 1, No. 3, 2002, pp. 241-274.

[11] Hein, S., Hohage, T., Koch, W., and Schoberl, J., "Acoustic Resonances in a High-lift Configuration", *Journal of Fluid Mechanics*, Vol. 582, 2007, pp: 179-202.

[12] Makiya, Sanehiro., Inasawa, A., and Asai, M., "Vortex Shedding and Noise Radiation from a Slat Trailing Edge", *AIAA Journal*, Vol. 48, No. 2, 2010, pp: 502-508.

[13] Souza D. S., Rodrguez, D., Simes, L. G. C, and Medeiros M. A. F., "Effect of an Excrescence in the Slat Cove: Flow-field, Acoustic Radiation and Coherent Structures", *Aerospace Science and Technology*, Vol. 44, pp: 108-115, 2015.

[14] Terracol, M., Manoha, E., and Lemoine, B., "Investigation of the Unsteady Flow and Noise Generation in a Slat Cove", *AIAA Journal*, Vol. 54, No. 2, 2016, pp: 469-489.

[15] Pagani, C. C., Souza, D. S., and Medeiros, M. F., "Slat Noise: Aeroacoustic Beamforming in Closed-Section Wind Tunnel with Numerical Comparison", *AIAA Journal*, Vol. 54, No. 7, 2016, pp: 2100-2115.

[16] Pagani, C. C., Souza, D. S., and Medeiros, M. F., "Experimental Investigation on the Effect of Slat Geometrical Configuration on Aerodynamic Noise", *Journal of Sound and Vibration*, Vol. 394, 2017, pp: 256-279.

[17] Pascioni, K. A., and Cattafesta, L. N., "An Aeroacoustic Study of a Leading-edge Slat: Beamforming and Far-field Estimation using Near-field Quantities", *Journal of Sound and Vibration*, Vol. 429, 2018, pp: 224-244.

[18] Pascioni, K. A., and Cattafesta, L. N., "Unsteady Characteristics of a Slat-cove Flow Field", *Physical Review Fluids*, Vol. 3, 2018, pp. 1-27.

[19] Li, L., Liu, P., Guo, H., Hou, Y., Geng, X., and Wang, J., "Aeroacoustic Measurement of 30P30N High-lift Configuration in the Test Section with Kevlar Cloth and Perforated Plate", *Aerospace Science and Technology*, Vol. 70, 2017, pp: 590-599.

[20] Li, L., Liu, P., Guo, H., Geng, X., Hou, Y., and Wang, J., "Aerodynamic and Aeroacoustic Experimental Investigation of 30P30N High-lift Configuration", *Applied Acoustics*, Vol. 132, 2018, pp: 43-48.

[21] Li, L., Liu, P., Xing, Y., and Guo, H., "Time-frequency Analysis of Acoustic Signals from a High-lift Configuration with two Wavelet Functions", *Applied Acoustics*, Vol. 129, 2018, pp: 155-160.

[22] Li, L., Liu, P., Xing, Y., and Guo, H., "Wavelet Analysis of the Far-Field Sound Pressure Signals Generated from a High-lift Configuration", *AIAA Journal*, Vol. 56, No.1, 2018, pp: 432-437.

[23] Horne, W. C., James, K. D., Arledge, T. K., Soderman, P. T., Field, M., Burnside, N., and Jaeger, S. M., "Measurement of 26%-scale 777 Airframe Noise in the NASA Ames 40- by 80 foot Wind Tunnel", AIAA 2005-2810, 2005.

[24] Streett, C., Casper, J., Lockard, D., Khorrami, M., Stoker, R., Elkoby, R., Wenneman, W., and Underbrink, J., "Aerodynamic Noise Reduction for High-Lift Devices on a Swept Wing Model", AIAA 2006-212, 2006.

[25] Imamura, T., Ura, H., Yokokawa, Y., Enomoto, S., Yamamoto, K., Hirai, T., Group, A. P., and Division, E. S., "Designing of Slat Cove Filler as a Noise Reduction Device for Leading-edge Slat", AIAA 2007-3473, 2007.

[26] Ura, H., Yokokawa, Y., Imamura, T., Ito, T., and Yamamoto, K., "Investigation of Airframe Noise from High Lift Configuration Model", AIAA 2008-19, 2008.

[27] Tao, J. and Sun, G., "A Novel Optimization Method for Maintaining Aerodynamic Performances in Noise Reduction Design", Aerospace Science and Technology, Vol. 43, 2015, pp. 415-422.

[28] Kamliya Jawahar, H., Showkat Ali, S. A., Azarpeyvand, M., Theunissen, R., and Silva, C., "Aeroacoustic Performance of Slat Cove Fillers", AIAA 2019-2440, 2019.

[29] Kamliya Jawahar, H., Azarpeyvand, M., and Silva, C., "Numerical Investigation of High-lift airfoil with Slat Cove Fillers", AIAA 2019-2439, 2019.

[30] Kamliya Jawahar, H., Azarpeyvand, M., Theunissen, R., and Silva, C., "Aerodynamic and Aeroacoustic Performance of Three-element High Lift Airfoil Fitted with Various Cove Fillers", AIAA 2018-3142, 2018.

[31] Kamliya Jawahar, H., Azarpeyvand, M., and Carlos R.Ilario. "Experimental Investigation of Flow Around Three-Element High-Lift Airfoil with Morphing Fillers", AIAA 2017-3364, 2017.

[32] Amaral, F. R. D., Junior, C. D. C. P., Himeno, F. H. T., Souza, D. S., and de Medeiros, M. A. F. "On closed-section wind-tunnel aeroacoustic experiments with a two-dimensional lifting body"., *Applied Acoustics*, Vol. 148, 2019, pp. 409-422.

[33] Barrett, R. V., "Design and Performance of a New Low Turbulence Wind Tunnel at Bristol University", *The Aeronautical Journal*, Vol. 88, No. 873, 1984, pp. 86-90.

[34] Liu, X., "Aerodynamic and Wake Development of Aerofoils with Trailing-Edge Serrations", University of Bristol, PhD Thesis, 2018.

[35] Sirovich, L., "Turbulence and the Dynamics of Coherent Structures-Part 1: Coherent Structures", *Quarterly of Applied Mathematics*, Vol. 45 No. 3, 1987, pp. 561-571.

[36] Pedersen, J. M., Srensen, J. N., and Meyer, K. E., "Analysis of Planar Measurements of Turbulent Flows", PhD Thesis, Technical University Denmark, MEK-FM-PHD, No. 2003-01, 2003.

[37] Meyer, K. E., Cavar, D., and Pedersen, J. M., "POD as Tool for Comparison of PIV and LES Data", 7th International Symposium on Particle Image Velocimetry, 2007, pp. 1-12.

[38] Olson, S., Thomas, F., and Nelson, R., "A Preliminary Investigation into Slat Noise Production Mechanisms in a High-lift Configuration", AIAA 2000-4508, 2000.

[39] Murayama, M., Nakakita, K., Yamamoto, K., Ura, H., and Ito, Y., "Experimental Study of Slat Noise from 30P30N Three-element High-lift Airfoil in JAXA Hard-wall Low-speed Wind Tunnel", AIAA 2014-2080, 2014.

[40] Richard, P. R., Wilkins, S. J., and Hall, J. W., "Flow Around a Leading Edge Slat Part 1: Turbulent Flow Statistics", ASME PVP2014-28316, 2014.

[41] Wilkins, S. J., Richard, P. R., and Hall, J. W., "Flow Around a Leading Edge Slat Part 2: Cove Flow Dynamics via Snapshot POD", ASME PVP2014-28315, 2014.

[42] Wilkins, S., Richard, P., and Hall, J. W., "Velocity Field Estimation Using Unsteady Wall Pressure Measurements in a Leading Edge Slat Flow", AIAA 2014-0896, 2014.

[43] Souza, D., Pagani, C., Rodriguez, D., and Medeiros, M., "Hydrodynamic Instability in the Generation of Slat Noise", *Procedia IUTAM*, Vol. 14, 2015, pp. 344-353.

[44] Richard, P. R., John Wilkins, S., and Hall, J. W., "Particle Image Velocimetry Investigation of the Coherent Structures in a Leading-Edge Slat Flow", *Journal of Fluids Engineering*, Vol. 140, No. 4, 2017, pp.1-11.

[45] Arndt, R. E. A., Long, D. F., and Glauser, M. N., "The Proper Orthogonal Decomposition of Pressure Fluctuations Surrounding a Turbulent Jet", *Journal of Fluid Mechanics*, Vol. 340, 1997, pp. 1-33.

[46] Oudheusden, B. W., Scarano, F., Hinsberg, N. P., and Watt, D. W., "Phase-Resolved Characterization of Vortex Shedding in the Near Wake of a Square-Section Cylinder at Incidence", *Experiments in Fluids*, Vol. 39, No. 1, 2005, pp. 86-98.